# A Vision-guided Dual Arm Sewing System for Stent Graft Manufacturing

Bidan Huang, Alessandro Vandini, Yang Hu, Su-Lin Lee, Guang-Zhong Yang, *Fellow, IEEE*

***Abstract*— This paper presents an intelligent sewing system for personalized stent graft manufacturing, a challenging sewing task that is currently performed manually. Inspired by medical suturing robots, we have adopted a single-sided sewing technique using a curved needle to perform the task of sewing stents onto fabric. A motorized surgical needle driver was attached to a 7 d.o.f robot arm to manipulate the needle with a second robot controlling the position of the mandrel. A learning-from-demonstration approach was used to program the robot to sew stents onto fabric. The demonstrated sewing skill was segmented to several phases, each of which was encoded with a Gaussian Mixture Model. Generalized sewing movements were then generated from these models and were used for task execution. During execution, a stereo vision system was adopted to guide the robots to adjust the learnt movements according to the needle pose. Two experiments are presented here with this system and the results show that our system can robustly perform the sewing task as well as adapt to various needle poses. The accuracy of the sewing system was within 2mm.**

## I. Introduction

Sewing is a delicate and laborious task. Though recent developments in robotics have brought changes to the sewing industry, some conventional hand stitches remain difficult to automate. The objective of our study is to automate sewing by teaching robots to create hand stitches. In particular, we focus on the task of sewing stents onto fabric for personalized stent graft manufacturing.

A stent graft is a tubular structure composed of fabric supported by a metal mesh called stent. It is commonly used during endovascular interventions for the reinforcement of the vessel wall in the presence of aneurysms. For stent grafts located near side branches, such as the renal arteries off the aorta, customisation to the patient anatomy is required, with fenestrations (openings) on the graft body to maintain the patency of these branches to vital organs. They often come at a significant cost in addition to a long manufacturing process; this is mainly due to the intensive manual craftsmanship involved in the process. As a consequence, patients are more likely to be subject to complications. Improved manufacturing of personalised stent grafts is therefore a critical unmet clinical demand and we are pursuing a robot-assisted manufacturing approach. This study focuses on the key process of sewing the stents onto a fabric tube, i.e. the graft. This is a challenging task for a robot, as hand sewing involves dexterous manipulation of the needle and complex bimanual motions. The stitching demands high accuracy and the fabric deformation must be handled in order to maintain the stitch quality. For this purpose, a robotic system is proposed in order to automate the hand sewing required during the stent graft manufacturing process (Figure 1).

B. Huang, A. Vandini, Y. Hu, S.-L. Lee and G.-Z. Yang are with the Hamlyn Centre for Robotic Surgery, Imperial College London, SW7 2AZ, London, UK (e-mail: b.huang@imperial.ac.uk). The project is supported by the EPSRC (EP/L020688/1).

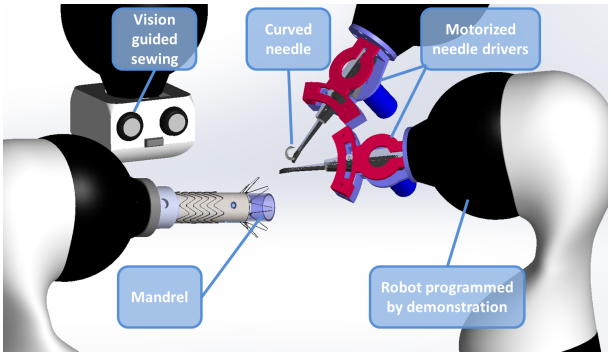


Fig. 1: The proposed robot sewing system for personalized stent graft manufacturing.

The main body of research has been in automated sewing for the textile industry. Intelligent robotic systems with multi-sensor feedback have been built to work in conjunction with traditional sewing machines. Important topics in this field include bimanual robotic sewing [10], fabric tension control, and seam tracking [20], [21]. To cope with environmental changes during the sewing process, various control strategies have been implemented, such as a fuzzy logic controller [9], a hybrid position/force control [10], or a leader/follower control strategy [19]. In addition, extensive research has been carried out on the design of sewing heads that are capable of sewing from a single side of the fabric, differing from conventional sewing requiring mechanisms at both sides of the fabric. These designs allow for sewing on a 3D surface. For example, KSL Keilmann (Lorsch, Germany) has developed various 3D stitching systems incorporating single-sided sewing heads onto KUKA manipulators for sewing fabric-reinforced structures of aircraft parts. However, these machines are designed for sewing large and heavy objects and are not suitable for delicate sewing for small objects with non uniform shapes.

As robotic assisted systems emerge in the field of minimally invasive surgery, automated suturing tasks are also widely investigated, providing the advantages of speed and accuracy. Medical suturing has two main tasks: tissue piercing and knot tying. For each task, procedural planning is performed according to well-established manual suture techniques [7], [8], [14] or by learning the skills from expert demonstrations [13], [16], [24]. Needle trajectories

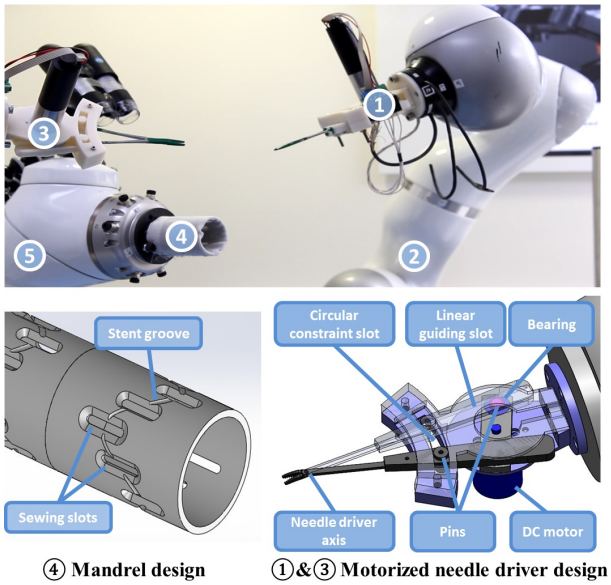


Fig. 2: Hardware designs. Top: (1) Needle driver A; (2) Robot 1; (3) Needle driver B; (4) Mandrel; (5) Robot 2. Bottom left: mandrel design (diameter 3.7cm). Bottom right: motorized needle driver design.

are also optimized, taking into account constraints in minimally invasive surgery, such as reducing tissue damage, port positioning, and surgical robot kinematics [15], [22].

Vision plays a key role in the achievement of a fully automated suturing task. To position the needle to the target point, both the needle posture and the target suturing plane posture are required. Iyer et al. [6] proposed a single-arm, single-camera system auto-suturing system, in which the area being sutured on was marked by round markers. In their method, the monocular pose measurement algorithm [12] was used for estimating the needle posture. Staub et al. [23] introduced the use of a 3D stereo system with visual servoing to improve the accuracy in aligning the needle with the target stitching point. Recently, an auto-suturing system with 2D camera guidance and a motorized Endo 360 suturing device was presented [11]. In this work, a method was presented to track the incision contour and automatically distributed equally-spaced stitches along the incision. Because of the nature of suturing tasks, all of these works used curved needles to perform single-sided sewing.

Inspired by these medical sewing approaches, we have developed a sewing system that makes use of surgical needle drivers and a curved needle. The use of a curved needle allows us to perform single-sided sewing, which simplifies the sewing system design (detailed in Section II). The proposed system is shown in Figure 1 and has three main components: 1) personalized stent graft sewing hardware design, including a mechanism to constrain the fabric (a mandrel) and a motorized surgical needle driver; 2) an easy-to-use interface to program the sewing skill (learning-from-demonstration) and 3) a vision system to guide the sewing and maintain stitch quality.

Compared to conventional sewing machines, our approach

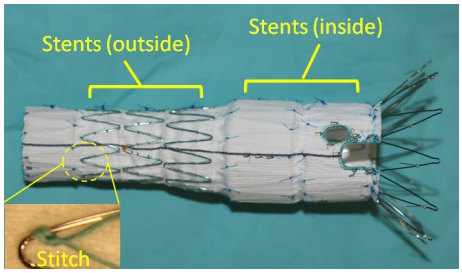


Fig. 3: A custom made stent graft with maximum diameter is 3.5 cm. Note that some stents are inside the graft and some are outside.

is more versatile. It benefits both from the flexibility of a medical suturing system and the stability of an engineered environment. It allows us to robotically sew stent grafts with patient specific designs, which are all currently hand-sewn (Figure 3). To the best of our knowledge, our system is the first autonomous single-sided sewing system that can create hand stitches for manufacturing. The main contribution of this work is threefold:

1) A dual arm robot sewing system that adaptively replicates hand stitches using visual information, in a hybrid programming by demonstration and programming by customized hardware design framework;
2) A robust needle pose estimation algorithm with shape and pose prior;
3) A novel hardware design (mandrel) to handle fabric deformation.

This paper presents the proposed system and is organized as follows. Section II describes our system, the hardware designs, and the software components. Section III shows the experiments conducted using this system and presents the results, followed by the discussion and conclusions in Section IV.

## II. System Overview

Our proposed sewing system for personalized stent graft manufacturing is shown in Figure 2. This system consists of two KUKA LWR 7 d.o.f robots: one (Robot 1) mounted with a motorized surgical needle driver (Needle Driver A) and the other (Robot 2) mounted with a 3D printed mandrel. The two robots play different roles in the task. Robot 1 is in charge of stitching: it delivers the needle to the stitching location and performs the stitches. Its motion is learnt from human demonstration and is cyclic. Robot 2 controls the sewing location: it places the mandrel at the pose required such that Robot 1 can stitch at the same location under its local frame. Another motorized surgical needle driver (Needle Driver B) is fixed next to the mandrel to re-grip the needle. The needle used is a 1/2 circular needle with 1cm diameter. A stereo vision system (two Logitech C930E cameras) is used to guide the sewing motion and to maintain stitch quality. The needle pose is tracked during the task and the learnt robot stitching motions are then amended online according to the current needle pose. In the following sections, we describe each component of the system in detail.

### A. Hardware Designs

*1) Motorized Needle Driver:* The fabric tubes used in stent grafts cannot be flattened into a single layer and hence conventional techniques of sewing a flat piece fabric are not applicable. A curved needle was used here with two motorized needle drivers as this allows for single-sided sewing and enhanced manipulation of needle. These needle drivers are widely used in laparoscopic surgery and are specially designed to firmly grasp the needle. DC motors are used to motorize the needle drivers, allowing the robot to control them. Figure 2 shows the motorized needle driver design. This design has two sets of slots: a pair of linear guiding slots, lying along the handles of the needle driver, and a circular constraint slot, coaxial with the needle driver. Therefore the motor rotation is mapped to the opening and closing movements of the needle driver. Bearings are used to reduce the friction of the pins moving in the slots.

*2) Mandrel:* The mandrel is a 3D printed hollow cylinder to support the fabric and the stents. The shape of the mandrel is optimized together with the fabric tube to fit each patient's anatomy. Stents can be sewn either inside or outside the fabric tube, according to the stent graft design. For stents inside, the grooves at the outer surface of the mandrel are used for fixing them. Slots are opened on the mandrel at the positions of stitches and allow for the needle to pierce through and sew the stent onto the fabric. For outside stents, the mandrel design is the same as before but the stents are loaded outside the fabric and fixed by string rings. Figure 2 shows a basic mandrel. Patient specific mandrels with bifurcations and fenestrations are designed based on the same principles, with different grooves and fabric tube shapes.

The mandrel movement controlled by Robot 2 is computed according to the mandrel design. After completion of one stitch, the mandrel is moved to align the next sewing slot with the Robot 1 trained piercing position (Section II B). The location of each sewing slot can be obtained from the mandrel CAD file and therefore the trajectory of Robot 2 can be programmed beforehand to cooperate with Robot 1. The personalization and manufacturing process of the fabric tube and the mandrel are out of the scope of this paper; however, regardless of the design of the mandrel, the stitching motions of Robot 1 are the same and the cooperation of the two robots remains in the same way.

### B. Learning sewing from human demonstration

Personalized stent grafts are mostly hand sewn; automating the process is difficult due to different patient anatomies. We tackle the problem with a dual arm system and by dividing the programming between two robots. While the personalized mandrel motion controlled by Robot 2 is programmed according to the mandrel design as explained in the previous section, the hand sewing motion of Robot 1 is learned from human demonstration.

*1) Human Demonstration of Stitching:* The first step is to recode the stitching motions from human demonstrations. The motion of finishing one stitch is called a stitching cycle. Figure 4 illustrates the motion steps in one stitching cycle.

At the beginning of the task, Needle Driver A firmly grips the needle end (Step a). Starting from an initial position, Needle Driver A approaches the mandrel and pierces the needle into the fabric (Step b). When the tip of the curved needle pierces out from the fabric, Needle Driver A releases the needle end (Step c). The needle stucks in the fabric with the same pose. Needle Driver A re-grips the needle at its tip and pulls it out from the fabric (Step d). Once the needle is completely out (Step e), Needle Driver A hands it over to Needle Driver B (Step f) and then moves to re-grip the needle end (Step g). Needle Driver A then moves back to the starting position and hence finishes a full stitching cycle. The mandrel then brings the next slot to the stitching location.

For all these steps, the task demonstrations were provided to the robots through the use of kinesthetic teaching. Robot 1 was put into gravity compensation mode and physically moved by the human demonstrator. Opening and closing of the needle driver was controlled by an electronic foot pedal. When grasped by a needle driver, the needle will not slip when interacting with the fabric as the motor of the needle driver provided a large enough torque for stability. Needle slippage could occur when the needle was released and re-gripped (Steps c and f) and this was compensated for by the vision system described in Section II C.

At the beginning of each demonstration, the needle was placed in the same pose relative to the needle driver; we refer to this pose as the *ideal piercing pose*. At Step e after the needle is completely pulled out from the fabric, the needle pose was adjusted to facilitate handing over to Needle Driver B; we refer to this pose as the *ideal hand over pose*. In the rest of the paper, we refer to both of these poses as the *ideal pose*. These ideal poses were first recorded under the needle driver frame and then transferred to the camera frame via hand eye calibration. This information is used 1) as the priors of needle pose estimation (Section II C) and 2) to generate adaptive robot motion online (Section II D).

All trajectories were recorded in 6 d.o.f with Euler angles $\{\alpha, \beta, \theta\}$ representing the orientation and $\{x, y, z\}$ representing the robot end effector position (i.e. the needle driver positions) at the frequency of 100Hz. When the needle driver is gripping the needle, an object centric approach of learning was taken. This is to say, the motion of the object, i.e. the needle, was learned rather than the movement of the robot. In our task, the needle movements for each stitching cycle should be exactly the same so that the quality of the sewing is maintained. This object centric approach allows for the generation of adaptive robot motions to perform the same stitch under different conditions, such as different needle poses. When the needle is released, the robot movements were learned such that it approaches the needle tip in the pose necessary to grip it firmly. To enable this, the stitch motions must be segmented into different phases.

*2) Motion Segmentation:* With all the collected training data (sewing trajectories), each trajectory was segmented to reflect the different phases of sewing and learn each phase

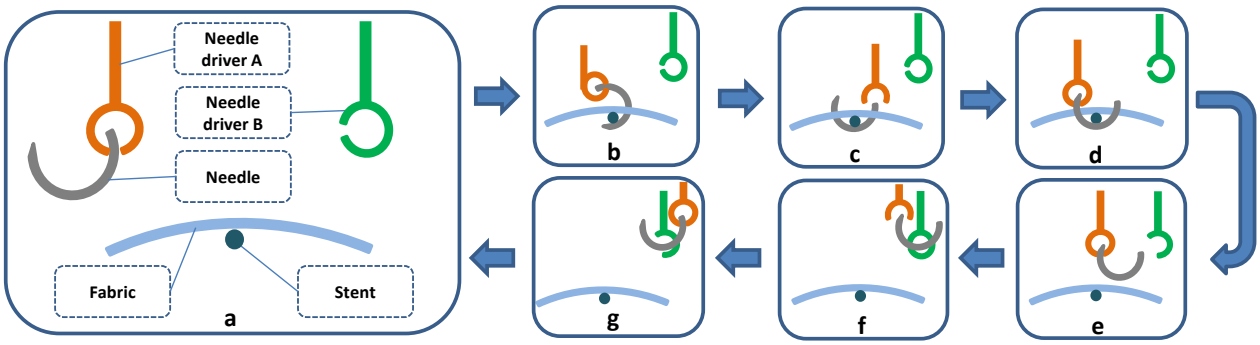


Fig. 4: Steps in one stitching cycle. a) Needle approaching fabric. b) Needle piercing the fabric. c) Needle rotating around the stent. d) Needle Driver A releasing the needle end and going to grip the needle head. e) Needle exits the fabric, approaching Needle Driver B. f) Needle Driver B gripping the needle in the middle, Needle Driver A releasing the needle. g) Needle Driver A gripping needle end, Needle Driver B releasing the needle.

TABLE I: Motion primitives of stitching

| Motion Primitives | Steps in Figure 6 | Needle Driver A status | Needle Driver B status | Needle status |
|---|---|---|---|---|
| 1. | a, b | Closed | Closed | With A |
| 2. | c | Open | Closed | With mandrel |
| 3. | d | Closed | Closed | With A |
| 4. | e | Closed | Open | With A |
| 5. | f | Open | Closed | With B |
| 6. | g | Closed | Open | With A |

independently. This segmentation was performed based on the relation between the needle and its driver: attached or detached. When the needle was attached to the driver, we took the object centric approach and learned the needle movement so that the needle can repeat this for stitching. When the needle was detached from the driver, the needle driver trajectory was learned in order to reach the proper location to re-grip the needle. Therefore, we use the status of the needle driver (opened or closed) to segment the trajectories. Table I shows the segments and their corresponding status. To align the data across different demonstrations, Dynamic Time Warping (DTW) [1] was applied. Each segment was then learned as a primitive movement and encoded by a Gaussian Mixture Model (GMM) [3] .

*3) Learning of Motion Primitives:* After segmentation of the data to a set of motion primitives, a model $\Omega$ was used to encode each primitive. Each primitive was represented in seven dimensions: one temporal value $\{t\}$ and a six d.o.f posture value $h = \{x, y, z, \alpha, \beta, \theta\}$. A joint distribution $p\{t, h \mid \Omega\}$ was built by using a GMM. The GMM was used because of its ability to encode non-linear data and its robustness in extracting constraints from noisy data [2], [5], [18].

With $N$ Gaussian components, the joint distribution $p$ was represented as:

$$p(t, h \mid \Omega) = \sum_{n=1}^{N} \pi_n p_n(t, h \mid \mu_n, \Sigma_n) \tag{1}$$

where $\pi_n$, $\mu_n$, $\Sigma_n$ and $p_n$ is the prior of the $n$-th Gaussian component, the corresponding mean, covariance, and the conditional probability density, respectively.

For the $n$-th Gaussian component, the mean and covariance $\mu_n$, $\Sigma_n$ are defined as:

$$\mu_n = \begin{pmatrix} \mu_{t,n} \\ \mu_{h,n} \end{pmatrix} \qquad \Sigma_n = \begin{pmatrix} \Sigma_{tt,n} & \Sigma_{th,n} \\ \Sigma_{ht,n} & \Sigma_{hh,n} \end{pmatrix} \tag{2}$$

Each motion primitive was encoded by one GMM. Before building the model, the training data was normalised to zero mean and variance of one. Initialized by using the K means, the values of $\mu$ and $\Sigma$ were estimated by the Expectation Maximization algorithm.

A smooth generalized trajectory was extracted using Gaussian Mixture Regression (GMR). With the $i$-th motion primitive model $\Omega_i$, a temporal value $t$ was used to query the trajectory $h$ at each time step. At a specific time step $\hat{t}$ the GMR estimated the conditional expectation value of the posture $\hat{h}$ as $\hat{\mu}_h$ with variance $\hat{\Sigma}_h$:

$$\hat{\mu}_h = \sum_{n=1}^{N} \beta_n(\hat{t})\, \hat{\mu}_{h,n} \qquad \hat{\Sigma}_{hh} = \sum_{n=1}^{N} \beta_n(\hat{t})^2\, \hat{\Sigma}_{hh,n} \tag{3}$$

where

$$\hat{\mu}_{h,n} = \mu_{h,n} + \Sigma_{th,n}(\Sigma_{tt,n})^{-1}(\hat{t} - \mu_{h,n}) \tag{4}$$

$$\hat{\Sigma}_{hh,n} = \Sigma_{hh,n} - \Sigma_{ht,n}(\Sigma_{tt,n})^{-1}\Sigma_{th,n} \tag{5}$$

and

$$\beta_n(\hat{t}) = \frac{\pi_n p(\hat{t} \mid \mu_{t,n}, \Sigma_{tt,n})}{\sum_{n=1}^{N} \pi_n p(\hat{t} \mid \mu_{t,n}, \Sigma_{tt,n})} \tag{6}$$

### C. Vision System

At the beginning of each stitch, the needle is gripped by the needle driver with a similar pose as the ideal piercing pose. After a few stitching cycles, there is a high chance that the needle pose, with respect to the needle driver, will deviate from its initial pose (Fig. 6). As the deviation accumulates, it can affect the quality of the stitches, e.g. an incorrect stitching location, and may even lead to task failure, e.g. the needle does not pierce the fabric. The learnt robot end effector (i.e. Needle Driver A) trajectory has to adapt to

changes in the needle pose in order to ensure the stitch quality. To tackle this problem, a stereo vision system was used to monitor the needle pose. Adaptive robot movements were then generated accordingly.

In the proposed system, the needle was first detected in each stereo image using the needle detection algorithm proposed in [17]. For this purpose, a feature image, i.e. $I_H$, based on the analysis of the eigenvalues of the Hessian matrix [25] was computed to enhance curvilinear structures in the image. Assuming that a calibrated imaging system was available, the 3D points of the needle's model defined by its ideal pose were projected in the image plane. This was performed in order to include prior information of the shape of the needle in the detection algorithm to make it more robust. Although the ideal pose of the needle was usually different from its true one due to slippage, it still represented a good estimate of the needle pose. Thus, small straight segments were detected in $I_H$, and only segments that were close to the projected needle and were of similar orientation were considered as parts of the needle. Finally, these segments were combined in order to create a continuous curve that represented the detected needle in the images. To improve the detection of the needle, the needle driver was also detected in the images using color-base segmentation in HSV space. This allowed for the reduction of false positive detection of needle segments which were mainly caused by the presence of the needle driver.

3D reconstruction of the needle was performed by triangulating the detected needle points of the stereo image pairs. However, in the current setup, a section of the needle was occluded in the images due to the presence of the needle driver. To overcome the occlusion and to estimate the new needle pose, a discretization of the reconstructed needle and the needle defined by the ideal pose was performed. Starting from the needle tip, points were sampled along the needle shape at a distance equal to the arch length of 1mm generating a set of equidistant 3D points, defined by $N_{ide}$ for the ideal and $N_{est}$ for the reconstructed needle, respectively. Finally, a rigid transformation $T_{ide}^{est}$ that best mapped the two set of points $N_{ide}$ and $N_{est}$, i.e. the new needle pose, was calculated using singular value decomposition (SVD). Calibration of the stereo camera was performed by using the OpenCV library[1]. The camera frame was registered to the robot frame by hand-eye calibration. This needle pose estimation algorithm is summarized in Algorithm 1.

### D. Online Adaptive Motion Generation

In order to sew continuously, the needle posture was examined at two key points of each stitching cycle: after re-gripping the needle tip (Motion Primitive 3) and after re-gripping the needle end (Motion Primitive 6). The motion primitives after these two examinations (Primitive 1 and 4 in Table I were then adapted to the new needle posture. The robot end effector adaptive posture $\hat{H}_{EE}$ at each time step $t$ was computed as:

[1]http://opencv.org/

**Algorithm 1** Needle Pose Estimation

**Input:** Rectified left and right images from stereo camera ($I_l$, $I_r$), camera parameters, ideal needle pose in camera frame ($N_{ide}$), 3D point model of needle ($M$)

**Output:** Current needle pose displacement ($T_{ide}^{est}$) w.r.t ideal pose

1: Extract feature images $I_H$ from $I_l$ and $I_r$
2: Project $M$ to $I_H$
3: Detect plausible needle segments in $I_H$
4: Construct needle shape by combining the segments
5: Needle driver detection by color-based segmentation
6: Refine needle shape by incorporating needle driver
7: 3D needle shape ($N_{est}$) reconstruction using triangulation of stereo images
8: Compute rigid transformation $T_{ide}^{est}$ between $N_{est}$ and $N_{ide}$ using SVD

$$\hat{H}_{EE}(t) = H_{EE}(t) \cdot T_{ide}^{EE} \cdot T_{ide}^{est}(t) \cdot T_{ide}^{EE^{-1}} \tag{7}$$

where $H_{EE}(t)$ represented the robot end effector posture at time $t$ in the learnt trajectory and $T_{ide}^{EE}$ the ideal needle pose with respect to the robot end effector during task demonstrations. With this equation, the adaptive motion was computed without re-learning or optimization.

## III. Experiments and Results

### A. Learning

Three sets of demonstrations were provided to the system. All demonstrations started from the same position and stitches performed on the same slot on the mandrel, with the needle piercing and exiting the fabric at the same spots. After data processing, the demonstrations were segmented into the six motion primitives as described in Table I. Needle pose estimation was implemented before Motion Primitives 1 and 4. The trajectories of these two primitives are recomputed according to the result of the needle pose estimations.

The number of Gaussians of each GMM was determined by using the Bayesian Information Criteria. Figures 5 b, d, f show the 2D projection of the built model of Motion Primitives 1-3. It can be seen from the model that the three primitives have different characteristics. The GMM of Motion Primitive 1 has large variance at the beginning and small variance at the end; this is due to the demonstrations finishing at the same stitch location and making the same stitch. A small variance means precise motions. For the same reason, Motion Primitive 2 has small variance both at the beginning and the end of the motion, while Motion Primitive 3 has small variance only at the beginning. These show that the GMM can effectively capture the constraints at each primitive and hence generate generalized trajectories for the robot to complete the task.

### B. Vision for needle pose estimation

Evaluation of the needle reconstruction algorithm was performed by estimating the 3D needle reconstruction error. This metric measured the distance between the reconstructed 3D shape and the ground truth shape of the needle. The

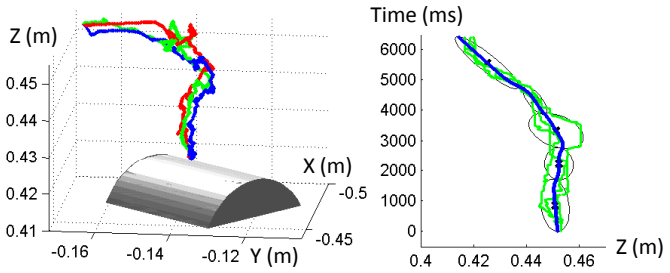


(a) Demonstrations of primitive 1 (b) 2D GMM representation

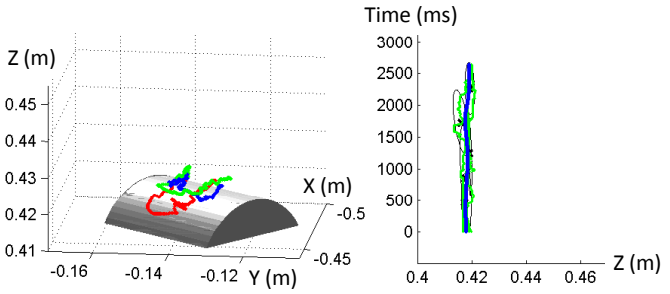


(c) Demonstrations of primitive 2 (d) 2D GMM representation

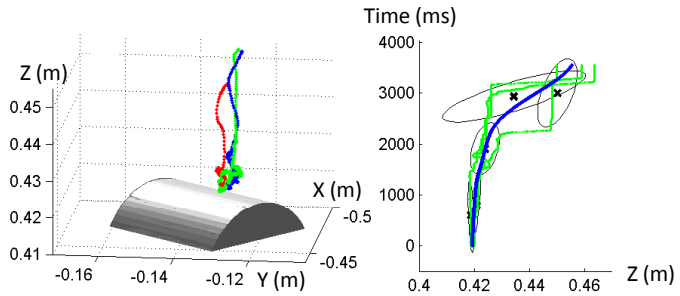


(e) Demonstrations of primitive 2 (f) 2D GMM representation

Fig. 5: Needle driver trajectories of human demonstrations and the learnt results of Motion Primitives 1-3. Left column: Multiple human demonstration trajectories. Each colour represents one demonstration. The cylinder represents the top of the mandrel. Right column: 2D representation of the learnt GMM models. Green lines are training data and the blue lines are the learnt trajectories. Black circles represent the 2D Gaussian contours.

ground truth was generated by triangulation of the manually segmented visible part of the needle in each stereo image. The 3D needle reconstruction error, i.e. $Dist(N_{gt}, N_{est})$, between the estimated needle, $N_{est}$, with respect to the ground truth shape, $N_{gt}$, was defined as:

$$Dist(N_{gt}, N_{est}) = \frac{1}{w+f}\left(\sum_{i=1}^{w} d_{min}(N_{gt}(i), N_{est}) + \sum_{j=1}^{f} d_{min}(N_{est}(j), N_{gt})\right) \quad (8)$$

where $w$ and $f$ are the cardinality of the set of points of $N_{gt}$ and $N_{est}$, respectively, and $d_{min}(N_{gt}(i), N_{est})$ is the Euclidean distance between the $i^{th}$ point of $N_{gt}$ to the closest point on $N_{est}$. The distance $Dist$ was also presented in [25].

TABLE II: Needle detection results

| Trials | 1 | 2 | 3 | 4 | 5 | 6 | 7 |
|---|---|---|---|---|---|---|---|
| Disp from ideal pose in Z (mm) | 0 | 5 | 10 | 0 | 0 | 0 | 0 |
| Disp from ideal pose in Yaw (deg) | 0 | 0 | 0 | -20 | -10 | 10 | 20 |
| Error (mm) | 0.46 | 0.50 | 0.52 | 0.68 | 0.56 | 0.47 | 0.36 |
| Stitch success | Y | Y | Y | N | Y | Y | Y |

Seven experiments were conducted to evaluate the accuracy of this algorithm. The experiments were carried out before the needle piercing, as needle piercing affects stitch quality the most. A set of seven poses were defined where the variations range between 10mm translation along the direction of the needle driver, and $\pm 20$ yaw rotation, respectively, with respect to the ideal piercing needle pose. We chose to vary in these two directions as we found that displacements along these two directions could largely affect the robot motions. The mean and standard deviation of the 3D needle reconstruction error for this experiment was $0.512 \pm 0.097$ mm (Table II). This shows the needle reconstruction allows for robust needle pose estimation and can provide accurate guidance to the robot autonomous sewing.

### C. Autonomous sewing

The result of each needle detection were used to recompute a piercing trajectory. With this adaptive trajectory, the robot was commanded to perform a stitch. The system successfully coped with the needle pose variations and completed a stitching cycle six times out of the seven attempts. At each experiment, we measured the displacement between the desired needle piercing locations and the actual locations. The largest displacement was less than $2mm$. The only failure that occurred was caused by the joint limit of the third joint of the robot ($\pm 120$), which was reached during the experiment involving a rotation of $-20$ of the needle. Figure 6 shows four snapshots of the experiments for four different poses including the ideal piercing needle pose.

The sewing system was tested by continuously running three stitching cycles without interruption. Two sets of experiments were run and were both successful. The robot movements of one stitching cycle are shown in Figure 7. After each needle detection, the current needle pose with respect to the ideal needle pose (piercing and handover) were recorded. Table III shows the displacements. As can be seen, the needle pose varies between each cycle. The robot successfully coped with these displacements and continuously made stitches on the fabric. Note that the displacement did not monotonically increase from one cycle to another, proving that the proposed system is able to avoid the displacement accumulation and therefore can continuously execute the sewing task. The accuracy of the stitch location was again within $2mm$. As for the previous experiments, we calculated the 3D needle reconstruction error for each needle detection.

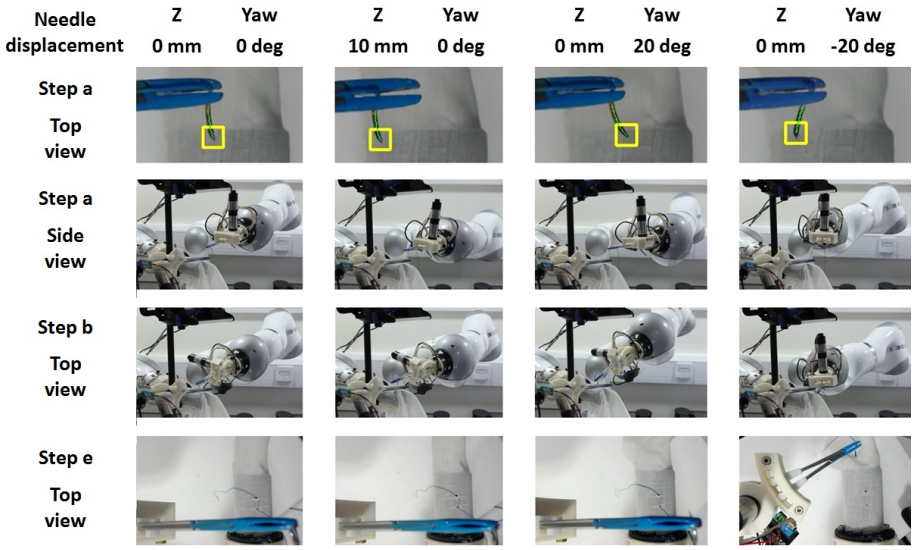


Fig. 6: Qualitative results of the task execution are shown for four different initial needle positions. Detection of the needle in the images is reported in the first row (frame of needle: X points downwards, Y points out of paper and Z points to left), while the robot adaptation during the task execution is shown in the second and third rows. The end of the task is in the last row.

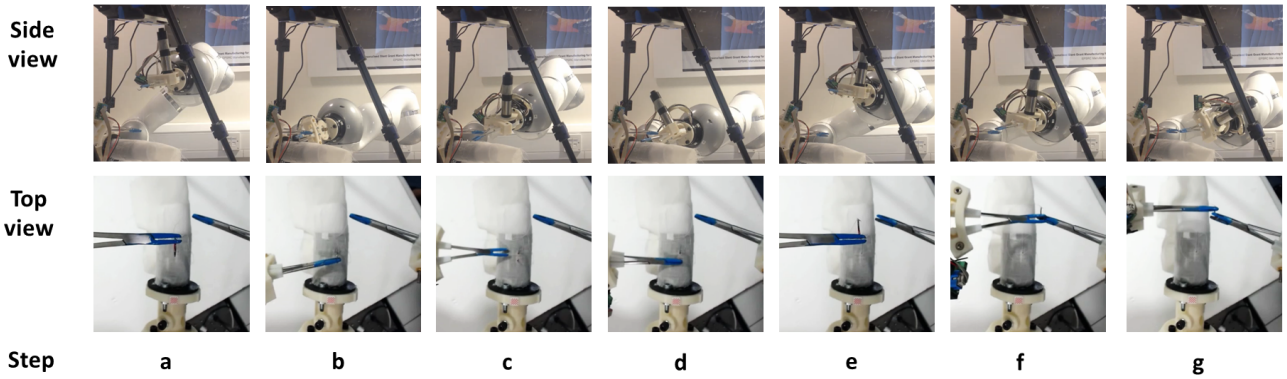


Fig. 7: One stitching cycle of the continuous sewing experiments. The letters at the bottom show their corresponding steps in Figure 4

.

TABLE III: Needle displacements during autonomous sewing. The needle was detected twice in one cycle: before piercing (P) and before handing over the needle (H). The detected current needle pose is compared with the ideal needle pose. The last column shows the 3D reconstruction errors of each needle detection.

| Exp 1 | | x (mm) | y (mm) | z (mm) | yaw (deg) | pitch (deg) | roll (deg) | Error (mm) |
|---|---|---|---|---|---|---|---|---|
| cycle1 | P | 0.77 | -0.74 | -0.69 | 5.78 | 4.81 | 1.31 | 0.56 |
| | H | -0.78 | -1.58 | -0.10 | 10.64 | 0.63 | 7.93 | 1.70 |
| cycle2 | P | -0.26 | 1.86 | -0.80 | 12.55 | -0.13 | 11.95 | 0.42 |
| | H | 0.00 | 1.15 | 1.37 | 1.52 | -6.16 | 6.43 | 1.37 |
| cycle3 | P | -0.34 | -0.33 | 1.50 | 6.45 | -8.94 | 3.92 | 0.35 |
| | H | -0.54 | 1.29 | 1.28 | 1.84 | -6.01 | 3.34 | 1.24 |
| Exp 2 | | | | | | | | |
| cycle1 | P | -0.15 | -0.57 | 0.74 | 1.95 | -11.04 | -4.21 | 0.45 |
| | H | -0.20 | 4.90 | 4.47 | 5.43 | -7.99 | 39.37 | 0.97 |
| cycle2 | P | -2.51 | -2.98 | 2.40 | 11.62 | -7.84 | 12.35 | 0.79 |
| | H | -0.73 | 1.33 | 0.90 | 6.81 | -6.41 | 7.44 | 1.51 |
| cycle3 | P | 1.24 | -1.07 | -1.15 | 10.81 | -0.88 | 5.65 | 0.84 |
| | H | -0.30 | 0.81 | 0.3 | 1.54 | -0.95 | -4.20 | 0.88 |

## IV. Discussion and Conclusion

In this paper a robotic system for sewing stent grafts is presented. Though inspired by surgical suturing, our sewing system is an adaptation of suturing techniques to a manufacturing application and is designed according to the task requirements and constraints. While automatic suturing systems focus on handling deformable tissues, our sewing system focuses on increasing the rigidity of the fabric by supporting it with a mandrel. In our experiments, we make an assumption that the fabric on a mandrel does not deform. According to the experimental results, this turns out to be a valid assumption. Furthermore, in a surgical suturing task stitches need to adapt to the medical conditions such as the width of the fissure. In comparison, our sewing system concentrates on making the same stitch and maintaining this stitch quality. To this end, a robust needle pose estimation algorithm was adopted to guide the robot. Across all our experiments, the overall mean and standard deviation of the 3D needle reconstruction error was $0.77 \pm 0.41$ mm. This enables the robots to sew in high accuracy.

In manufacturing, users may need to program the robot without an robot expert and we have shown that a learning from demonstration approach can be used to program a robot to perform sewing movements. The robustness of the method was shown quantitatively by three experiments. We showed that our system is able to accomplish the sewing task effectively. The limited workspace caused by the robot joint limits can be overcome by formulating the task as bimanual cooperation and optimizing the task priority in the null space [4].

One important direction of our future work is thread manipulation. Currently, the thread is manually tightened at the end of each stitch. Visual tracking of the thread will be introduced to the system in the future. The system currently works in an open-loop manner for needle adaptation, i.e. needle movements are not tracked and corrected in real time. Though the system is able to work robustly, the stitch quality has not yet met the medical requirements of a stent graft. Tracking the needle in real-time and implementing an enhanced visual servoing algorithm is desired to increase the sewing accuracy.

The system presented in this paper is a promising initial study of robot sewing with hand stitches. With the same system setup, this can be easily extended to create different hand stitches, including those for fenestration edge finishing and knot tying. Applications of the presented system and methods are not limited only to stent graft sewing; it is also a promising technique for automating robotic suturing.

## REFERENCES


[1] Donald J Berndt and James Clifford. Using dynamic time warping to find patterns in time series. In *KDD Workshop*, volume 10, pages 359–370. Seattle, WA, 1994.

[2] Sylvain Calinon, Florent Guenter, and Aude Billard. On learning, representing, and generalizing a task in a humanoid robot. *Systems, Man, and Cybernetics, Part B: Cybernetics, IEEE Transactions on*, 37(2):286–298, 2007.

[3] D.A. Cohn, Z. Ghahramani, and M.I. Jordan. Active learning with statistical models. *Journal of Artificial Intelligence Research*, 4:129–145, 1996.

[4] Yang Hu, Bidan Huang, and Guang-Zhong Yang. Task-priority redundancy resolution for co-operative control under task conflicts and joint constraints. In *Intelligent Robots and Systems (IROS), 2015 IEEE/RSJ International Conference on*. IEEE, 2015.

[5] Bidan Huang, Sahar El-Khoury, Miao Li, Joanna J. Bryson, and Aude Billard. Learning a real time grasping strategy. In *Robotics and Automation (ICRA), 2013 IEEE International Conference on*, pages 593–600, 2013.

[6] Srikrishna Iyer, Thomas Looi, and James Drake. A single arm, single camera system for automated suturing. In *Robotics and Automation (ICRA), 2013 IEEE International Conference on*, pages 239–244. IEEE, 2013.

[7] Russell C Jackson and M Cenk Cavusoglu. Needle path planning for autonomous robotic surgical suturing. In *Robotics and Automation (ICRA), 2013 IEEE International Conference on*, pages 1669–1675. IEEE, 2013.

[8] Ankur Kapoor and Russell H Taylor. A constrained optimization approach to virtual fixtures for multi-handed tasks. In *Robotics and Automation, 2008. ICRA 2008. IEEE International Conference on*, pages 3401–3406. IEEE, 2008.

[9] Panagiotis Koustoumpardis, Nikos Aspragathos, and Paraskevi Zacharia. *Intelligent robotic handling of fabrics towards sewing*. INTECH Open Access Publisher, 2006.

[10] Makoto Kudo, Yasuo Nasu, Kazuhisa Mitobe, and Branislav Borovac. Multi-arm robot control system for manipulation of flexible materials in sewing operation. *Mechatronics*, 10(3):371–402, 2000.

[11] Simon Leonard, Kyle L Wu, Yonjae Kim, Alexandra Krieger, and Peter CW Kim. Smart tissue anastomosis robot (star): A vision-guided robotics system for laparoscopic suturing. *Biomedical Engineering, IEEE Transactions on*, 61(4):1305–1317, 2014.

[12] Diego Lo, Paulo RS Mendonça, Andy Hopper, et al. Trip: A low-cost vision-based location system for ubiquitous computing. *Personal and Ubiquitous Computing*, 6(3):206–219, 2002.

[13] Hermann Mayer, Faustino Gomez, Daan Wierstra, Istvan Nagy, Alois Knoll, and Jürgen Schmidhuber. A system for robotic heart surgery that learns to tie knots using recurrent neural networks. *Advanced Robotics*, 22(13-14):1521–1537, 2008.

[14] Florent Nageotte, Philippe Zanne, Michel De Mathelin, and Christophe Doignon. A circular needle path planning method for suturing in laparoscopic surgery. In *Robotics and Automation, 2005. ICRA 2005. Proceedings of the 2005 IEEE International Conference on*, pages 514–519. IEEE, 2005.

[15] Florent Nageotte, Philippe Zanne, Christophe Doignon, and Michel De Mathelin. Stitching planning in laparoscopic surgery: Towards robot-assisted suturing. *The International Journal of Robotics Research*, 2009.

[16] Nicolas Padoy and Gregory D Hager. Human-machine collaborative surgery using learned models. In *Robotics and Automation (ICRA), 2011 IEEE International Conference on*, pages 5285–5292. IEEE, 2011.

[17] Hedyeh Rafii-Tari, Alessandro Vandini, Lin Zhang, Archie Hughes-Hallett, and Guang-Zhong Yang. Vision-guided learning by demonstration for adaptive surgical robot control. In *Hamlyn Symposium*, pages 39–40, 2015.

[18] Carol E Reiley, Erion Plaku, and Gregory D Hager. Motion generation of robotic surgical tasks: Learning from expert demonstrations. In *Engineering in Medicine and Biology Society (EMBC), 2010 Annual International Conference of the IEEE*, pages 967–970. IEEE, 2010.

[19] Johannes Schrimpf, Magnus Bjerkeng, and Geir Mathisen. Velocity coordination and corner matching in a multi-robot sewing cell. In *Intelligent Robots and Systems (IROS 2014), 2014 IEEE/RSJ International Conference on*, pages 4476–4481. IEEE, 2014.

[20] Johannes Schrimpf and Lars Erik Wetterwald. Experiments towards automated sewing with a multi-robot system. In *Robotics and Automation (ICRA), 2012 IEEE International Conference on*, pages 5258–5263. IEEE, 2012.

[21] Johannes Schrimpf, Lars Erik Wetterwald, and Morten Lind. Real-time system integration in a multi-robot sewing cell. In *Intelligent Robots and Systems (IROS), 2012 IEEE/RSJ International Conference on*, pages 2724–2729. IEEE, 2012.

[22] Siddarth Sen, Animesh Garg, David V. Gealy, Stephen McKinley, Yiming Jen, and Ken Goldberg. Automating multiple-throw multilateral surgical suturing with a mechanical needle guide and sequential convex optimization. In *Robotics and Automation (ICRA), IEEE International Conference on (in-press)*. IEEE, 2016.

[23] Christoph Staub, Takayuki Osa, Alois Knoll, and Robert Bauernschmitt. Automation of tissue piercing using circular needles and vision guidance for computer aided laparoscopic surgery. In *Robotics and Automation (ICRA), 2010 IEEE International Conference on*, pages 4585–4590. IEEE, 2010.

[24] Jur Van Den Berg, Stephen Miller, Daniel Duckworth, Humphrey Hu, Andrew Wan, Xiao-Yu Fu, Ken Goldberg, and Pieter Abbeel. Superhuman performance of surgical tasks by robots using iterative learning from human-guided demonstrations. In *Robotics and Automation (ICRA), 2010 IEEE International Conference on*, pages 2074–2081. IEEE, 2010.

[25] T. van Walsum, S. A M Baert, and W.J. Niessen. Guide wire reconstruction and visualization in 3DRA using monoplane fluoroscopic imaging. *IEEE Trans. Med. Imag.*, 24(5):612–623, 2005.